Check for updates

Radioactive cesium-137 removal from contaminated wastewater using bio-based activated carbon from cassava rhizomes enhanced with copper hexacyanoferrate

Kanyanat Tawatbundit,[a] Sudarat Issarapanacheewin, [ID] *[a] Witsanu Katekaew,[a] Nikom Prasertchiewchan,[a] Wilasinee Kingkam[b] and Poonnaphob Sopapan[c]

The presence of radioactive cesium-137 (Cs-137) contaminated in wastewater poses serious environmental and health concerns. This study presents the synthesis and characterization of activated carbon derived from cassava rhizomes (CRAC), further composited with copper hexacyanoferrate (CuHCF), for the removal of Cs-137 from actual wastewater. The cassava rhizome was treated with potassium permanganate ($KMnO_4$) *via* a hydrothermal carbonization process (HTC) before being pyrolyzed to produce high-surface-area activated carbon, which served as a support matrix for CuHCF nanoparticles known for their high selectivity toward cesium ions. The synthesis of copper hexacyanoferrate and cassava rhizome (CuHCF/CRAC) composites was achieved through the hydrothermal method. Batch adsorption tests were performed to assess the removal effectiveness of Cs-137 at a concentration of 10 000 Bq L^{-1} from real wastewater. The incorporation of 5% w/w of $KMnO_4$ into the CuHCF/CRAC composites resulted in optimal Cs-137 removal efficiency, exceeding 99%. The improved adsorption capability was mainly attributed to the oxidative modification introduced by $KMnO_4$, which generated aromatic ($C=C$), hydroxyl ($-OH$), and carboxylate ($-COO^-$) groups, which improved electrostatic interactions with positively charged Cs ions. Adsorption isotherm and kinetic analyses revealed that the Freundlich isotherm and pseudo-second-order kinetic models provided the best fit for Cs-137 uptake across all tested adsorbents. The CuHCF/CRAC(5) composite demonstrated excellent reusability, maintaining high Cs ion removal efficiencies (>97%) over five consecutive adsorption–regeneration cycles following acid washing with 0.1 M HCl. Furthermore, adsorption efficiency was notably enhanced under neutral to alkaline pH conditions. These results highlight the strong potential of CuHCF-based activated carbon composites for practical applications in radioactive wastewater treatment.

Introduction

Electric Arc Furnace Dust (EAFD) is a by-product generated during steel production in electric arc furnaces (EAF), particularly when melting scrap steel. It is considered hazardous waste due to its heavy metal compositions and environmental risks but it also contains valuable metals, including iron (Fe) and zinc (Zn), that make it a potential secondary resource.[1–3] Recently in Thailand, EAFD has been discovered to be contaminated with cesium-137 (Cs-137) due to the accidental contamination of scrap metals used in the process by radioactive Cs element.[4] Cs-

137 is a radioisotope of significant concern, noted for its long half-life of 30.17 years, the emission of gamma rays, and its solubility in water.[5] Akharawutchayanon *et al.*[5] examined the efficacy of different solvents in the lixiviation process for extracting Cs-137 from radioactively contaminated EAFD. Nevertheless, this study produced secondary contaminated Cs-137 liquid waste. Chemical precipitation, solvent extraction, ion exchange, electrochemical separation, and adsorption are some of the potential methods that could be utilized to efficiently remove Cs-137 from liquid radioactive waste solutions.[4,6]

Adsorption technology is acknowledged as an efficient technique for eliminating Cs-137 radioactive pollutants from liquid waste. This benefit arises from the production of low secondary waste, cost-effectiveness, high efficiency, and stability.[7,8] The adsorbent, which includes many categories such as biosorbents, organic adsorbents, and inorganic adsorbents, is essential in adsorption technology.[9,10] Activated carbon (AC) derived from biomass or agricultural wastes have attracted

[a]Nuclear Safety Technology and Radioactive Waste Management Center, Thailand Institute of Nuclear Technology (Public Organization), Ongkharak, Nakhon Nayok, 26120, Thailand. E-mail: sudarat@tint.or.th

[b]Nuclear Technology Research and Development Center, Thailand Institute of Nuclear Technology (Public Organization), Ongkharak, Nakhon Nayok, 26120, Thailand

[c]Department of Radiological Technology, Faculty of Medicine Vajira Hospital, Navamindradhiraj University, Bangkok, 10300, Thailand

significant interest as adsorbents owing to their cost-effectiveness, abundant availability, eco-friendly characteristics, elevated specific surface area, and homogeneous pore size distribution.[11] AC is synthesized *via* the processes of carbonization and activation. Chemical activation agents such as KOH, $ZnCl_2$, H_3PO_4, and $KMnO_4$ are extensively utilized to achieve a porous structure and enhance its adsorption properties.[12] Potassium permanganate ($KMnO_4$) is extensively utilized to improve the porosity, surface area, and surface functionality of adsorbent materials, which efficiently adsorb positively charged Cs ions.[13] In our previous study, Sudarat *et al.*[14] modified commercial activated carbon (CAC) using $KMnO_4$ at different concentrations of 1%, 3%, and 5% w/v. The maximum adsorption of Cs-137 achieved with $KMnO_4$ concentration of 5% w/v, attributed to the carboxyl (–COOH) and carbonyl (>C=O) functional groups present on the CAC surface.

Cassava rhizome (CR) refers to the underground stem portion of the cassava plant (*Manihot esculenta*), which connects the above-ground stem to the tuberous roots. While cassava is primarily cultivated for its starchy roots, the rhizome itself is a less commonly utilized part but still has potential value, especially in biomass and waste-to-energy applications.[15,16] CR serves as a sustainable and cost-effective precursor to produce activated carbon due to its high carbon content, making it an attractive foundational material for adsorbents used in environmental remediation.[17,18] Nevertheless, the application of CR is limited due to its higher moisture content. Therefore, to enhance its utilization efficiency, a hydrothermal carbonization pretreatment process is necessary.[19,20] Various bio-based activated carbons have been investigated for their effectiveness in removing Cs ions from aqueous solutions. Khandaker *et al.*[21] examined the adsorptive removal of cesium from aqueous solutions using oxidized bamboo charcoal. The maximum adsorption capacity for Cs ions was found to be 55.25 mg g^{-1}. Moloukhia *et al.*[22] developed biomass activated carbon derived from coconut shell and altered the surface using H_2O_2 and HNO_3. The adsorption capacity was determined to be 60.00 mg g^{-1} for Cs ions. However, biomass activated carbon shows limited adsorption capacity for certain radionuclides, including Cs-137, primarily because it lacks selective functional groups and possesses weak ion-exchange properties. The identified limitations hinder its effective use in the treatment of radioactive wastewater.[23] To improve the efficiency of activated carbon in wastewater treatment, composite materials featuring effective adsorbents for the removal of Cs-137, such as metal hexacyanoferrate (MHCFs), have been suggested.[24]

Metal hexacyanoferrates represent a category of coordination compounds that arise from the interaction between metal ions and hexacyanoferrate anions, typically denoted as $[Fe(CN)_6]^{3-}$ or $[Fe(CN)_6]^{4-}$. The compounds exhibit a porous structure, possess ion-exchange properties, and demonstrate selective adsorption capabilities for specific metal ions, particularly radioactive cesium (Cs^+).[25] Copper hexacyanoferrate (CuHCF) represents a specific category of metal hexacyanoferrate compound, characterized by the coordination of copper ions with hexacyanoferrate anions. This material features a porous, crystalline structure and is recognized for its selective ion

exchange capabilities, particularly for cesium ions (Cs^+), which renders it valuable in the fields of nuclear waste remediation and electrochemical applications.[26] Several studies are investigating the composite of CuHCF and carbon-based adsorbents for removing radioactive cesium from aqueous solutions. Abd-Elhamid *et al.*[27] synthesized sugarcane bagasse and copper(II) ferrocyanide composite for the extraction of cesium from aqueous solution. The composite has a maximum cesium removal efficiency of 126.00 mg g^{-1}.

This study aims to synthesize and characterize CRAC/CuHCF composites to enhance the efficiency of Cs-137 removal from contaminated wastewater. Adsorption kinetics were investigated to elucidate the mechanism of Cs-137 uptake on the surface of the adsorbents. The pseudo-first-order and pseudo-second-order kinetic models were applied to describe the adsorption behavior. Additionally, the Langmuir, Freundlich, and Temkin isotherm models were employed to evaluate the adsorption equilibrium in relation to the concentration of Cs-137. The research focuses on optimizing the synthesis process, analyzing the physicochemical properties of the composites, and assessing their adsorption capacity and selectivity toward Cs-137. The findings are expected to contribute to the development of a cost-effective, sustainable, and efficient strategy for treating radioactive wastewater and addressing the environmental challenges associated with radioactive contamination. Moreover, the potential interference from coexisting ions such as Na^+, K^+, and Mg^{2+} was considered in this study. We carried out tests using actual EAFD leachate, which naturally has various competing ions, including alkali and alkaline earth metals. The results demonstrated that the composite materials maintained high selectivity for Cs^+ even under these competitive conditions. These findings confirm the material's robustness and practical applicability for Cs-137 removal from complex wastewater systems.

Experimental

Chemicals and precursor materials

Cassava rhizome (CR) used in this study was obtained from Uthai Thani province, Thailand. The modification process of CR involved the use of potassium permanganate ($KMnO_4$) that was purchased from KemAus™ Inc., Australia. Copper(II) nitrate ($Cu(NO_3)_2$; Ajax Finechem, Australia) and potassium hexacyanoferrate(III) ($K_3[Fe(CN)_6]$; Sigma Aldrich, United States) were used as precursors to synthesis of pure CuHCF. Sodium chloride (NaCl) was employed as the solution in the determination of the point of zero charge (pH_{pzc}), which was supplied by QRёc Co., Ltd, New Zealand. The pH adjustments were carried out using hydrochloric acid (HCl; RCl Labscan Ltd, Ireland) and sodium hydroxide (NaOH; KemAus™ Inc., Australia). Electric arc furnace dust (EAFD) contaminated with radioactive Cs-137 was obtained from a steel manufacturing facility.

Preparation of activated carbon from cassava rhizome (CRAC)

The cassava rhizome (CR) was thoroughly cleaned using distilled water, air-dried under sunlight, and then cut into

pieces. 10 g of CR was mixed with potassium permanganate ($KMnO_4$) at concentrations of 0%, 1%, and 5% w/w in 10 mL of distilled water. The samples were pretreatment through immersion for 24 hours at room temperature. Subsequently, the samples underwent to treatment in a hydrothermal autoclave at a temperature of 120 °C and a pressure of 0.15 MPa for 6 hours. The samples were then allowed to cool to room temperature. After that, the samples were subjected to three washes with distilled water. All samples were contained in lidded crucibles and calcined at 400 °C for 1 hour. The activated carbon (AC) derived from CR were designated as CRAC(0), CRAC(1), and CRAC(5), corresponding to treatment with $KMnO_4$ concentrations of 0%, 1%, and 5% w/w, respectively. The calculation of the percent yield of CRAC was performed using eqn (1).[28]

$$\text{Yield } (\%) = \frac{\text{mass}_0}{\text{mass}_1} \times 100 \qquad (1)$$

where mass_0 and mass_1 represented the weight of activated carbon (g) and the weight of raw material (g), respectively.

Synthesis of pure CuHCF and CuHCF/CRAC composites

The co-precipitation technique was employed for the synthesis of pure CuHCF. Initially, 120 mL of 0.1 mol L^{-1} $Cu(NO_3)_2$ and 120 mL of 0.05 mol L^{-1} $K_3[Fe(CN)_6]$ were added dropwise to 60 mL of deionized water while maintaining continuous stirring for 3 hours. Subsequently, the sample underwent treatment in an ultrasonic bath for 20 minutes to improve particle dispersion. Following the reaction, the suspension was maintained at room temperature for 24 hours to facilitate complete precipitation. The solution had three washes with deionized water to remove any remaining impurities. The solid product was separated through centrifugation at 6000 rpm for 5 minutes. The sample was dried at 40 °C for 48 hours, resulting in the formation of a brown CuHCF powder as the final product.

The synthesis of the CuHCF/CRAC composite was achieved successfully through a hydrothermal method. The composite of copper hexacyanoferrate (CuHCF) and cassava rhizome activated carbon (CRAC) was executed at a weight ratio of 1 : 1. 0.5 g of CRAC and 0.5 g of CuHCF were added together with 30 mL of deionized water. The solution was subsequently placed into a Teflon-lined stainless-steel autoclave for a hydrothermal reaction at 120 °C for 10 hours. Following this, the solution was separated via centrifugation and was then dried in an oven at 105 °C for 12 hours. The composites were designated as CuHCF/CRAC(0), CuHCF/CRAC(1), and CuHCF/CRAC(5), based on the varying concentrations of $KMnO_4$ used in the process.

Adsorption experiment

A solution containing radioactive Cs-137, with an activity concentration of 10 000 Bq L^{-1}, was prepared through the leaching of contaminated electric arc furnace dust (EAFD) with deionized water and was subsequently utilized in batch adsorption studies. In the experiment, 0.05 g of CRAC, CuHCF, and CuHCF/CRAC composites were each added to 10 mL of EAFD solution and stirred continuously for 24 hours. Following the adsorption process, the solution was separated by

centrifugation. Each adsorption experiment was conducted in triplicate to ensure the accuracy of the results. The radioactivity concentration of Cs-137 in the solution was determined using gamma spectrometry with a High-Purity Germanium (HPGe) detector (model GEMC40, Ametek Ortec, USA). The concentration of radioactive cesium-137 (w, mg L^{-1}) was then calculated based on eqn (2)–(4).[29]

$$C = \frac{\lambda \times A_{av} \times w}{M} \qquad (2)$$

$$w = \frac{C \times M}{\lambda \times A_{av}} \qquad (3)$$

$$\lambda = \frac{\ln 2}{t^{1/2}} = \frac{0.693}{t^{1/2}} \qquad (4)$$

where C represents the radioactivity concentration (Bq L^{-1}), M denotes the atomic mass (g mol^{-1}), λ is the decay constant of the radioisotope (s^{-1}), and A_{av} refers to Avogadro's number (6.02×10^{23} nuclei mol^{-1}). The equilibrium adsorption capacity (Q_e), the percentage removal efficiency (R) of Cs-137, and the distribution coefficient (K_d) were calculated using eqn (5)–(7), respectively.[30]

$$Q_e = \frac{(C_0 - C_e)}{M} \times V \qquad (5)$$

$$R \ (\%) = \frac{(C_0 - C_e)}{C_0} \times 100\% \qquad (6)$$

$$K_d = \frac{(C_0 - C_e)}{C_e} \times \frac{V}{M} \qquad (7)$$

where C_0 and C_e are the initial and equilibrium concentrations of Cs-137 (mg L^{-1}), M is the mass (g) of the adsorbent, and V is the volume of the Cs-137 solution (L).

Reusability of CuHCF/CRAC composites

To assess the reusability of the adsorbent, CuHCF/CRAC(5) composites were subjected to multiple adsorption–regeneration cycles. In each cycle, 0.05 g of adsorbent was added to 10 mL of EAFD solution and stirred continuously for 24 h. After Cs-137 adsorption, the spent adsorbent was regenerated by desorption using 0.1 M of HCl, followed by thorough washing with deionized water until the pH stabilized between 6 and 7. The regenerated adsorbent was then dried at 110 °C for 6 h and reused in subsequent adsorption cycles. Adsorption efficiency and the number of regeneration cycles were systematically recorded throughout the process.

Characterization

The morphology, particle size, and elemental composition of all samples were characterized using field-emission scanning electron microscopy (FESEM, SU8230, Hitachi, Japan) coupled with energy-dispersive X-ray spectroscopy (EDS, Ultim max, Oxford Instruments, UK). Fourier transform infrared spectroscopy (FT-IR) was investigated functional groups and chemical bonding characteristics, using a Thermo Scientific Nicolet iS50

spectrometer (USA). The phase composition and crystalline structure of the samples were analyzed *via* X-ray diffraction (XRD) using a Bruker D8 Advance apparatus. X-ray photoelectron spectroscopy (XPS) was utilized to determine the elemental composition and chemical states of surface atoms, using a Kratos Analytical Ltd AXIS Ultra ULD system (UK). The specific surface area and pore size distribution were evaluated using the Brunauer–Emmett–Teller (BET) and the Barrett–Joyner–Halenda (BJH) methods, respectively, with a Micromeritics 3Flex analyzer. Nitrogen adsorption–desorption isotherms were recorded at −196 °C following a degassing process, in which the samples were heated to 120 °C under vacuum for 15 hours to eliminate residual moisture.

Results and discussion

The yield percentage of hydrochar

The yield percentage was determined using eqn (1), and the calculated values are summarized in Table 1. The increase in yield percentages of CRAC(0), CRAC(1), and CRAC(5) with rising $KMnO_4$ concentrations, reaching 21.27%, 21.34%, and 29.05%, respectively, is consistent with the expected behaviour of biomass during hydrothermal carbonization. This enhancement is attributed to the thermal degradation of biomass components such as cellulose, hemicellulose, and lignin, which is intensified by the presence of $KMnO_4$ as an oxidizing agent. The pretreatment facilitates more efficient conversion of biomass into hydrochar, thereby improving yield.[31] Furthermore, the thermal decomposition of $KMnO_4$ resulted in the formation of manganese oxide (MnO_2) and potassium oxide (K_2O), which exhibit thermal stability in the temperature range of 300–400 °C, thereby enhancing the yield percentage of hydrochar.[32]

FESEM-EDS analysis

The SEM images in Fig. 1 illustrate the surface morphology and microstructural characteristics of CRAC, CuHCF, and CuHCF/CRAC composites. The CRAC(0) morphology displays a comparatively smooth surface, a porous structure, and fragmented particles. The hydrothermal carbonization (HTC) process enhances the development of a fragmented and porous structure. In the process of HTC, biomass undergoes treatment at high temperature and pressure with water, resulting in the partial decomposition and reorganization of its organic components.[33,34] The addition of $KMnO_4$ at a concentration of 1% w/w during HTC notably affects the surface morphology. $KMnO_4$ acts as a strong oxidizing agent, facilitating partial oxidation and surface fragmentation, which results in a more porous structure with increased surface roughness.[35] Increasing
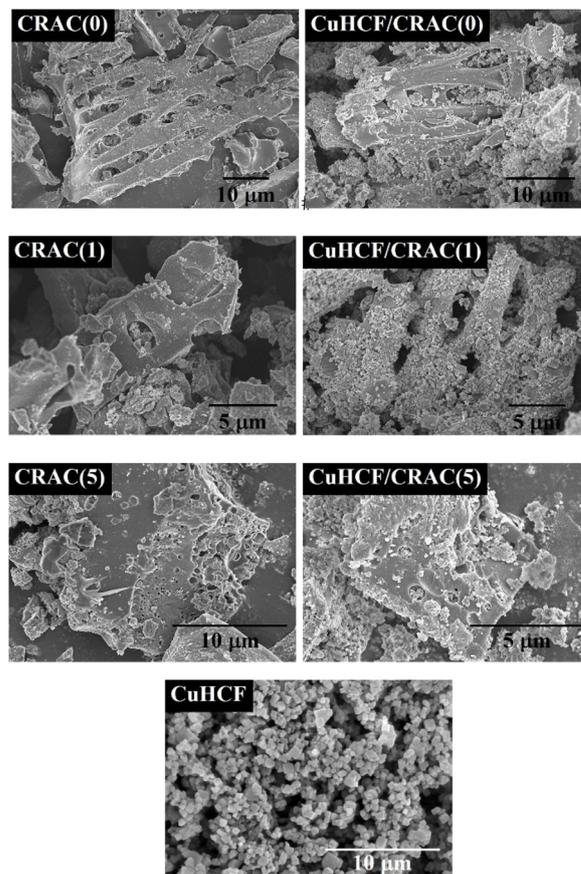

Fig. 1 FESEM images of CuHCF, CRAC and CuHCF/CRAC composites.

the $KMnO_4$ concentration to 5% w/w resulted in the formation of smaller and more uniform pores, suggesting a more compact and refined porous structure in comparison to the 1% w/w concentration of $KMnO_4$. The CuHCF nanoparticles exhibited a smooth surface and a well-defined cubic lattice structure, with particle sizes ranging from 32 to 152 nm. SEM analysis revealed that pure CuHCF displayed crystalline and aggregated particle formations, with a relatively low porosity compared to the CuHCF/CRAC composites. In composite samples, CuHCF is well-dispersed, especially in CuHCF/CRAC(1) and CuHCF/CRAC(5), enhancing the interaction sites for Cs-137. The combination of CRAC's porous structure and CuHCF's selective adsorption properties results in superior material performance.

The EDS results presented in Table 2 provide insights into the elemental composition of CuHCF, CRAC(5), and CuHCF/CRAC(5) composites. The CuHCF contains a high percentage of carbon

Table 1 The yield percentage of cassava rhizome activated carbon with addition of $KMnO_4$

CRAC(0)	CRAC(1)	CRAC(5)
21.27%	21.34%	29.05%

Table 2 Elemental compositions of CuHCF, CRAC(5), and CuHCF/CRAC(5) composites

Materials	Elemental compositions (wt%)							
	C	N	O	K	Mn	Ca	Fe	Cu
CuHCF	56.9	21.1	5.7	0.7	—	—	4.0	11.7
CRAC(5)	72.8	—	14.0	11.5	1.5	0.1	—	—
CuHCF/CRAC(5)	58.4	7.5	15.2	5.2	1.2	3.0	3.0	6.4

(56.9%) and nitrogen (21.1%), which reflects the presence of cyanide ligands in its hexacyanoferrate framework.[36] The presence of copper (11.7%) and iron (4.0%) is consistent with the Cu–Fe coordination characteristic of CuHCF.[37,38] Additionally, the relatively low levels of oxygen (5.7%) and potassium (0.7%) suggest minial contamination or hydration in the sample.[39] The CRAC(5) exhibits a high carbon content (72.8%), confirming its identity as a carbon-rich adsorbent.[40] The presence of oxygen (14.0%) suggests the existence of surface functional groups such as hydroxyl and carboxyl, which can enhance adsorption capacity.[41] The relatively high potassium content (11.5%) likely originates from plant-based precursors or chemical agents used during activation.[42,43] Trace amounts of manganese (1.5%) and calcium (0.1%) may be attributed to residual minerals naturally present in the biomass source.[43] The EDS results confirm the successful formation of the CuHCF/CRAC(5) composite, with elemental contributions from both CuHCF and CRAC(5). The presence of Cu, Fe, and N in the composite indicates effective integration of CuHCF, while the retained porosity and oxygen-rich surface from CRAC(5) enhance its adsorption potential for radioactive cesium.

FTIR analysis

The functional groups of all samples were characterized using FTIR spectroscopy, as shown in Fig. 2, with spectra recorded in the wavenumber range of 650–4000 cm^{-1}. Fig. 2a presents the

Fig. 2 FTIR spectra of (a) CRAC and (b) CuHCF/CRAC composites.

FTIR spectra of CRAC samples prepared with varying concentrations of KMnO$_4$ at 0%, 1%, and 5% w/w. The spectrum of CRAC displays shoulder peaks at approximately 1565 cm^{-1} and 1375 cm^{-1}, corresponding to the C=C stretching vibrations of aromatic rings and the –C–OH bending vibrations of hydroxyl groups, respectively.[44–46] A distinct carbonyl (C=O) peak at around 1667 cm^{-1} is observed in CRAC(0) but disappears in the spectra of KMnO$_4$-modified activated carbons (CRAC(1) and CRAC(5)). This disappearance is attributed to the strong oxidizing nature of potassium permanganate, which reacts with hydroxyl and carboxyl groups, thereby reducing the carboxyl content.[47] Additionally, a weakened peak near 1120 cm^{-1} corresponds to C–O stretching vibrations,[48,49] while the peak at 873 cm^{-1} is associated with C–H bending vibrations.[50] Fig. 2b shows FTIR spectra of all CuHCF/CRAC composites. The FTIR spectra of the CuHCF/CRAC composites exhibit sharp peaks at approximately 2171 cm^{-1} and 2100 cm^{-1}, which correspond to Fe^{3+}–C≡N–Cu^{2+} and Fe^{2+}–C≡N–Cu^{2+} stretching vibrations, respectively. These peaks confirm the presence and uniform distribution of iron oxidation states within the synthesized materials.[51] A peak at 1400–1604 cm^{-1} is attributed to carboxylate (–COO^{-}) vibrations, indicating antisymmetric stretching of the functional group.[30] A broad peak near 3381 cm^{-1} corresponds to O–H stretching vibrations. This indicates the presence of hydroxyl groups. The 1348 cm^{-1} region is more commonly associated with C–O bending.[52]
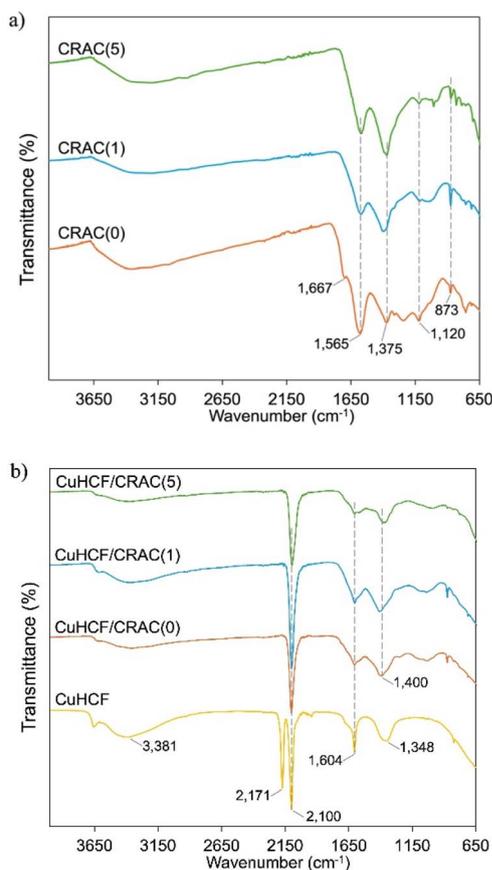
XRD analysis

Fig. 3 shows the XRD patterns that provide the crystalline phases present in the CRAC, CuHCF, and CuHCF/CRAC composites. The XRD patterns of CRAC samples exhibit distinct and broad peaks at approximately 24.3° and 43.4°, which correspond to the (002) and (100) planes, respectively. These peaks are indicative of a graphitized carbon structure, suggesting partial ordering within the carbon matrix.[53,54] The diffraction peak observed at approximately 14.8°, corresponding to the (110) plane of cellulose, indicates the presence of residual cellulose in the cassava rhizome-derived activated carbon.[55,56] Peaks at approximately 26.6° and 27.8°, assigned to the (111) and (101) planes, respectively, are attributed to elemental silicon (Si) and silicon dioxide (SiO$_2$, quartz).[57,58] Additionally, diffraction peaks at approximately 29.3°, 31.6°, 35.9°, 39.4°, 47.5°, and 48.5°, corresponding to the (104), (006), (110), (113), (018), and (116) planes, respectively, confirm the presence of calcium carbonate (CaCO$_3$), which originates from the natural mineral content of cassava rhizome, as identified by JCPDS card no. 05-0586.[58,59] Furthermore, diffraction peaks observed at approximately 30.1° and 38.3°, corresponding to the (−220) and (−330) planes, respectively, indicate the presence of calcium silicate (CaSiO$_3$), as referenced by JCPDS card no. 42-0550.[58]

Following the modification with KMnO$_4$, the original diffraction peaks continued to be observable. New peaks associated with MnO$_2$ were also produced because of the reduction of KMnO$_4$. The analysis of CRAC(1) and CRAC(5) revealed peaks at around 18.3°, 25.7°, and 37.8°, which align with the (200),
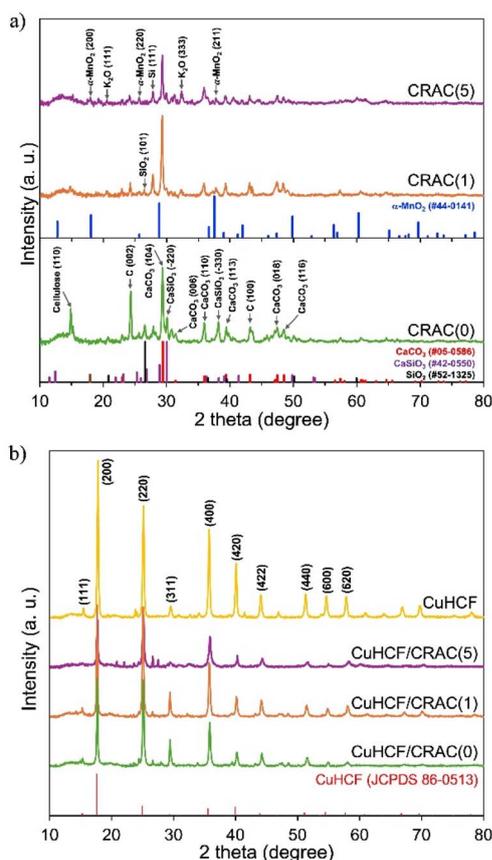
Fig. 3 XRD spectra of (a) CRAC and (b) CuHCF/CRAC composites.

(220), and (211) planes, respectively. This observation confirms the existence of α-MnO$_2$ in a tetragonal phase, as referenced in JCPDS no. 44-0141.[60] A diffraction peak observed at 40.7°, corresponding to the (220) plane, validated the synthesis of MnO (JCPDS card no. 07-0230).[61] Additional peaks at $2\theta = 23.3°$ and 32.5°, attributed to the (111) and (333) planes, were indicative of K$_2$O.[62]

Fig. 3b presents the XRD spectra of CuHCF, which displays characteristic diffraction peaks at approximately 15.5°, 17.6°, 24.7°, 29.6°, 35.6°, 39.9°, 44.3°, 51.3°, 54.4°, and 57.8°. These peaks are indexed to the (111), (200), (220), (311), (400), (420), (422), (440), (600), and (620) planes, respectively, in accordance with JCPDS card no. 86-0513.[63] The CuHCF/CRAC composites also exhibit distinct diffraction peaks of CuHCF, confirming that the composites retain a face-centered cubic (FCC) crystal structure with high crystallinity. The presence of vacant sites within this lattice facilitates the mobility of Cs$^+$ ions, thereby enhancing their insertion into the crystalline framework.[37]

XPS analysis

Fig. 4 shows the XPS spectra used to analyze the elemental composition and oxidation states of the samples. Fig. 4a shows the survey data of CRAC(5), CuHCF, and CuHCF/CRAC(5), which include characteristic peaks of Cu 2p, Fe 2p, Mn 2p, O 1s, N 1s, Ca 2p, K 2p, and C 1s. The Cu 2p spectra of CuHCF and

CuHCF/CRAC(5) are illustrated in Fig. 4b, revealing a prominent Cu 2p$_{3/2}$ peak at approximately 932, 935, and 937 eV, assigned to Cu$^+$, Cu^{2+}, and the Cu^{2+} satellite peak, respectively. The Cu 2p$_{1/2}$ peaks appeared at 953, 955, and 957 eV, corresponding to Cu$^+$, Cu^{2+}, and the Cu^{2+} satellite peak, respectively.[39,64] Fig. 4c depicts the Fe 2p$_{3/2}$ spectra of CuHCF and CuHCF/CRAC(5), confirming the coexistence of Fe^{2+} (708 eV) and Fe^{3+} (710 eV). The Fe 2p$_{1/2}$ peaks at 721 and 723 eV further verify the presence of Fe^{2+} and Fe^{3+}, respectively. Additionally, CuHCF exhibited Fe^{3+} satellite peaks at 711 and 724 eV.[39,64]
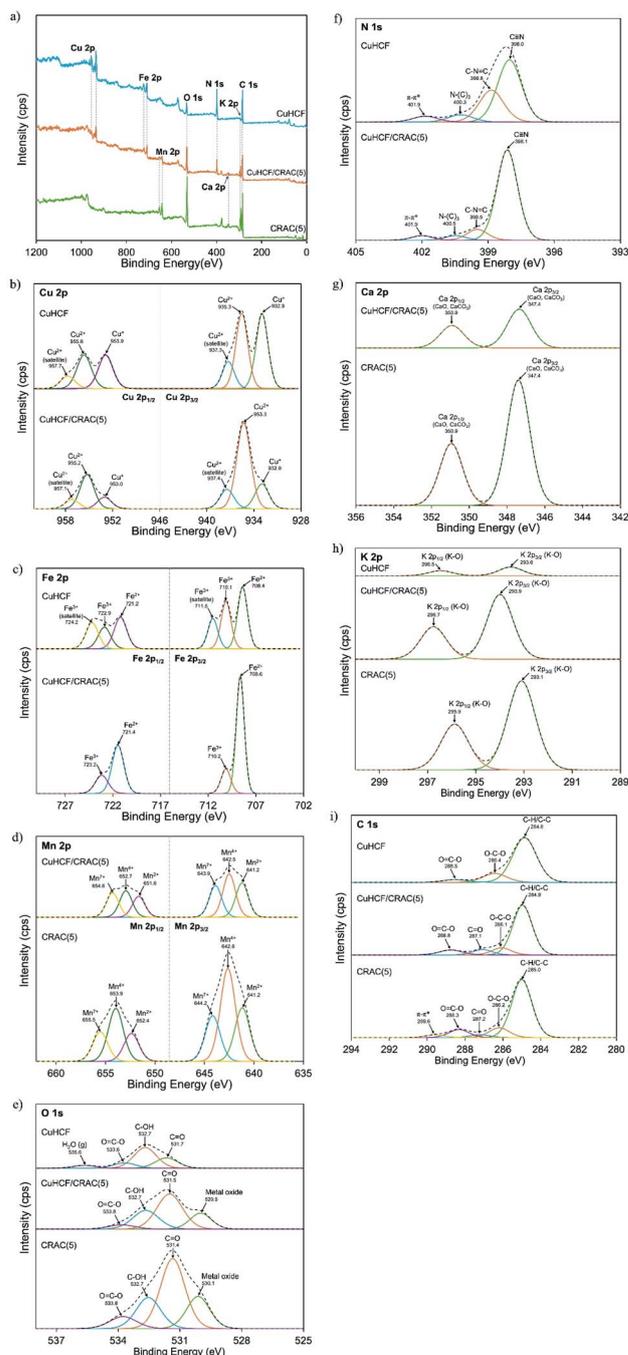

Fig. 4 XPS spectra of all samples. (a) Survey spectra, (b) Cu 2p, (c) Fe 2p, (d) Mn 2p, (e) O 1s, (f) N 1s, (g) Ca 2p, (h) K 2p, and (i) C 1s regions.

Fig. 4d presents the Mn 2p spectra of CRAC(5) and CuHCF/CRAC(5), showing Mn $2p_{3/2}$ peaks at approximately 641, 642, and 644 eV, and Mn $2p_{1/2}$ peaks at around 652, 654, and 656 eV, respectively.[65,66] The peaks near 641 eV (Mn $2p_{3/2}$) and 652 eV (Mn $2p_{1/2}$) are attributed to Mn^{2+} species in MnO. Peaks at approximately 642 eV and 654 eV correspond to Mn^{4+} in MnO_2, while those at 644 eV and 656 eV are associated with Mn^{7+} in $KMnO_4$.[67] The O 1s spectra (Fig. 4e) of the three adsorbents exhibited peaks at approximately 531, 532, and 533 eV, corresponding to $C=O$, C–OH, and $O=C-O$ bondings, respectively. Furthermore, CRAC and CuHCF/CRAC(5) showed an additional peak at 530 eV, indicating Mn–O bonds derived from $KMnO_4$ modification, whereas CuHCF displayed a peak at 535 eV, attributed to H_2O in gas phase.[68–70] Fig. 4f shows the N 1s spectra of CuHCF and CuHCF/CRAC(5), with peaks observed at 398, 399, 400, and 401 eV, corresponding to $C\equiv N$, $C-N=C$, $N-(C)_3$, and $\pi-\pi^*$ excitation, respectively.[39,71] Fig. 4g displays the Ca 2p spectra of CRAC(5) and CuHCF/CRAC(5), where peaks at 347 eV (Ca $2p_{3/2}$) and 350 eV (Ca $2p_{1/2}$) were assigned to CaO and $CaCO_3$ groups, supporting the XRD analysis results that confirmed the presence of CaO and $CaCO_3$ phases.[72,73] The K 2p spectra of the three adsorbents (Fig. 4h) exhibited peaks at around 293 eV (K $2p_{3/2}$) and 296 eV (K $2p_{1/2}$), corresponding to K–O groups.[74,75] Finally, Fig. 4i illustrates the C 1s spectra of the three adsorbents, with peaks at 284, 286, and 288 eV, assigned to C–H/C–C, O–C–O, and $O=C-O$, respectively. Additionally, $C=O$ was observed at 287 eV for CRAC and CuHCF/CRAC(5), while CRAC(5) also exhibited a $\pi-\pi^*$ excitation peak at 289 eV.[70,76] Overall, the detailed XPS analysis confirmed the successful incorporation of CuHCF onto CRAC, the coexistence of multiple oxidation states of transition metals, and the presence of functional groups that contribute to the enhanced adsorption properties of the composite materials.

Specific surface area and pore size distribution

The BET surface area, total pore volume, and average pore diameter of CuHCF, CRAC, and CuHCF/CARC composites are presented in Table 3. The CuHCF nanoparticles exhibited the largest BET surface area and pore volume, measuring 316.89 m^2 g^{-1} and 38.51 cm^3 g^{-1}, respectively, indicating substantial adsorption capacity. CRAC alone exhibits low porosity. However, modification with $KMnO_4$ significantly enhances the pore volume and increases the average pore size, with improvements becoming more pronounced as the $KMnO_4$ concentration increases. This improvement is due to the strong oxidative effect of $KMnO_4$, which enhances the breakdown of organic components in the precursor and generated of MnO_2 particles. These MnO_2 deposits contribute to increased surface roughness, reduced particle size, and elevated surface area.[77] The CuHCF/CRAC composites show significantly improved surface area and pore volume compared to CRAC alone, though not as high as pure CuHCF. The pore diameter varies, with CuHCF/CRAC(5) showing a decrease compared to CuHCF/CRAC(0) and CuHCF/CRAC(1) composites, possibly due to structural densification. The incorporation of CuHCF into activated carbon resulted in a significant enhancement of the

Table 3 BET surface area, total pore volume, and average pore diameter of CRAC, CuHCF, and CuHCF/CRAC composites

Sample	BET surface area (m^2 g^{-1})	Total pore volume (cm^3 g^{-1})	Average pore diameter (nm)
CuHCF	316.89	38.51	1.35
CRAC(0)	2.80	0.0072	2.47
CRAC(1)	2.35	0.0121	3.71
CRAC(5)	6.02	0.0370	4.26
CuHCF/CRAC(0)	61.54	0.1176	2.23
CuHCF/CRAC(1)	64.29	0.1508	2.51
CuHCF/CRAC(5)	88.31	0.1548	1.66

BET surface area, primarily due to the increased porosity and the introduction of additional active adsorption sites. The presence of CuHCF not only reduced the particle size but also improved key surface properties, including surface area, pore volume, and average pore diameter. Consequently, the composited activated carbon exhibited enhanced adsorption performance, offering a well-balanced combination of physical structure and chemical functionality that effectively improved cesium ion removal efficiency.

The BET surface area and total pore volume of pristine CuHCF decreased after compositing with CRAC due to partial pore blocking and surface coverage. However, adsorption
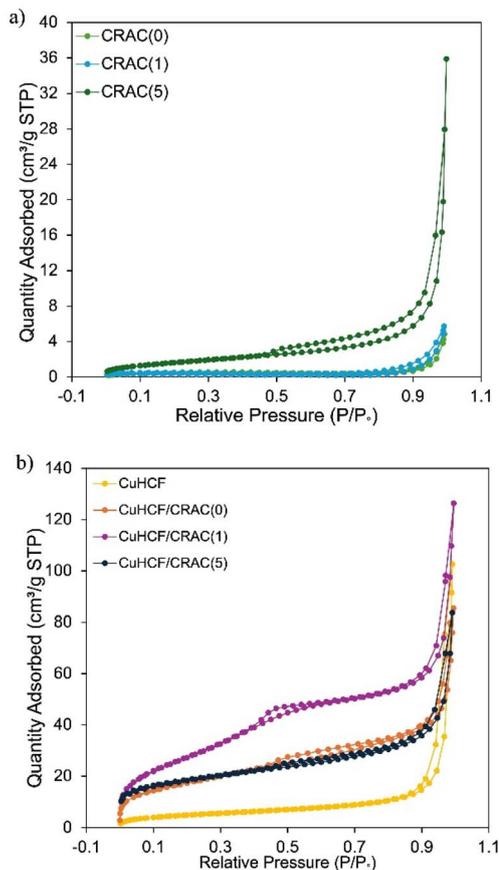

Fig. 5 N_2 adsorption–desorption isotherms of (a) CRAC and (b) CuHCF/CRAC composites.

performance in selective ion systems is not solely dictated by surface area. In this study, Cs$^+$ adsorption is primarily governed by ion-exchange and coordination within the open-framework structure of CuHCF rather than physical adsorption.[37,38] Supporting CuHCF on activated carbon improves nanoparticle dispersion, structural stability, and prevents aggregation, ensuring accessibility of Cs$^+$ exchange sites. Despite reduced BET values, the CuHCF/CRAC composites exhibited superior Cs$^+$ removal efficiency compared to pristine CuHCF, highlighting that chemical affinity and selectivity outweigh surface area effects. Similar trends have been reported, where decreased surface area after composite formation did not compromise adsorption performance due to enhanced active site utilization and mass transfer.[78–80]

The N$_2$ adsorption–desorption isotherms and pore sizes distribution of CRAC, CuHCF, and CuHCF/CRAC composites was illustrated in Fig. 5 and 6, respectively. As shown in Fig. 5a and b, all samples exhibited type IV nitrogen adsorption–desorption isotherms, characteristic of mesoporous materials. Moreover, the hysteresis loops observed were classified as type H4, which is typically associated with narrow slit-like pores. The presence of H4-type hysteresis in both CRAC and CuHCF/CRAC composites suggests the existence of microporous–mesoporous structures, likely arising from the aggregation of plate-like particles or the formation of narrow pore channels. The pore

size distribution profiles of all samples (Fig. 6a and b) exhibit multiple peaks within the range of 2 to 50 nm, confirming the presence of mesoporous structures. These distributions reflect the coexistence of various mesopore sizes, which may result from differences in material composition, surface modification, or structural aggregation.[81–83]

Influence of contact time on the Cs-137 adsorption behavior

The adsorption equilibrium was investigated by mixing 0.05 g of adsorbent with 10 mL of Cs-137 solution under continuous stirring. The concentration of Cs-137 in the solution was monitored at various time intervals: 1, 2, 3, 4, 5, 6, 12, 18, 24, 30, 36, 42, and 48 hours, to assess the adsorption kinetics and determine the equilibrium point. A rapid adsorption of Cs-137 was observed during the initial 6 hours, followed by a gradual increase. Equilibrium was attained at 24 hours for CRAC(1), CuHCF and all CuHCF/CRAC composites. In contrast to CRAC(0) and CRAC(5), which required nearly 42 hours to achieve adsorption equilibrium. The quicker saturation of CuHCF and CuHCF/CRAC composites occurred in the first 6 hours, that can be attributed to their porous framework and the abundance of active sites that enhance ion mobility, resulting in strong interactions between Cs ions and the available surface vacancies. Beyond this stage, the adsorption rate slowed as the active sites became progressively occupied, reducing the number of accessible sites. Once equilibrium was approached, the Cs-137 concentration in the solution stabilized, and the adsorption rate leveled off at a steady state,[84,85] as shown in Fig. 7.

Radioactive Cs-137 removal efficiency

The Cs-137 removal efficiency performance of CRAC, CuHCF, and CuHCF/CRAC composites was shown in Fig. 8a. The results demonstrate that the incorporation of CuHCF significantly enhances the adsorption of cesium ions. Among the tested materials, CuHCF/CRAC(5) exhibited the highest removal efficiency at 99.15%, followed by CuHCF/CRAC(1) at 98.58%, CuHCF/CRAC(0) at 98.22%, and pure CuHCF at 98.09% after 24 hours of adsorption. Corresponding adsorption capacities were
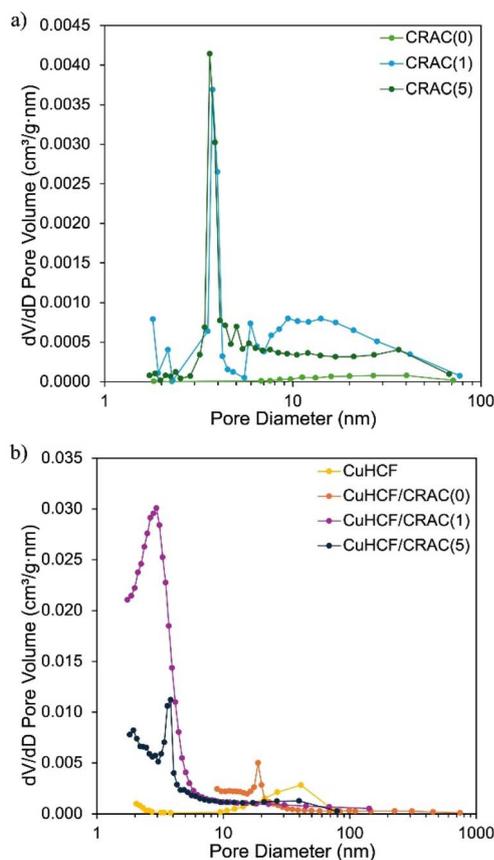

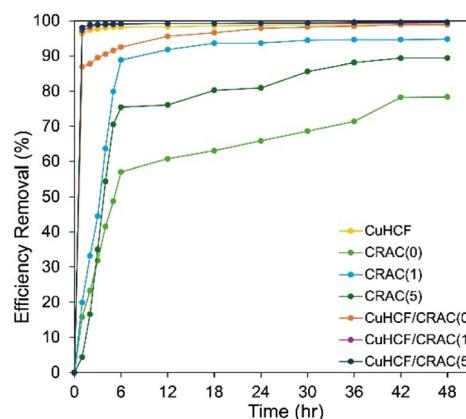Fig. 6 Pore size distribution of (a) CRAC and (b) CuHCF/CRAC composites.

Fig. 7 Effect of contact time of all samples on the adsorption of Cs-137.
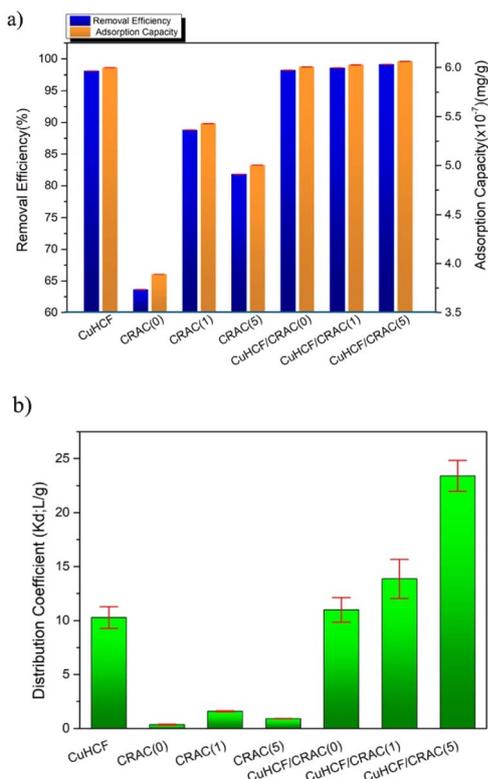
Fig. 8 (a) Removal efficiency and adsorption capacity and (b) distribution coefficient of Cs-137 solution using the CRAC, CuHCF, and CuHCF/CRAC composites over 24 hours.

6.06×10^{-7}, 6.03×10^{-7}, 6.01×10^{-7}, and 6.00×10^{-7} mg g^{-1}, respectively. In comparison, the Cs-137 removal efficiencies of CRAC(0), CRAC(1), and CRAC(5) were 63.63%, 88.81%, and 81.82%, with respective adsorption capacities of 3.89×10^{-7}, 5.43×10^{-7}, and 5.00×10^{-7} mg g^{-1}. The improved performance of CRAC(1) and CRAC(5) is attributed to KMnO$_4$-mediated pore structure enhancement. However, excessive KMnO$_4$ led to MnO$_2$ accumulation, which obstructed pore accessibility and reduced adsorption efficiency. The superior performance of CuHCF/CRAC(5) synthesized *via* hydrothermal treatment is

likely due to the synergistic effects of multiple factors. First, MnO$_2$ formed on the CRAC surface contributes to cesium adsorption, as manganese dioxide is known for its high affinity toward cesium ions.[86,87] Second, hydrothermal treatment effectively removes impurities from the activated carbon surface, improving composite purity and enhancing the accessibility of active sites.[88–90] Third, the composite materials introduce additional functional groups, such as manganese oxides, carboxyl, and carbonyl groups, which provide more active sites for cesium ion trapping, thereby increasing adsorption capacity.[14,86,87] The small difference in Cs-137 removal efficiency between pristine CuHCF and CuHCF/CRAC(5) can be attributed to the intrinsically high ion-exchange selectivity of CuHCF toward cesium ions, which dominates the overall adsorption behavior. In this system, CuHCF acts as the primary active phase for Cs$^+$ capture and already achieves near-complete cesium removal due to its strong affinity. Therefore, the incorporation of CRAC mainly serves as a supporting matrix that improves material dispersion and provides additional adsorption sites, resulting in only a marginal enhancement in removal efficiency. The adsorption performance of the materials was assessed using the distribution coefficient (K_d), which quantifies the affinity of the adsorbent for target ions in solution, as shown in Fig. 8b. A higher K_d value indicates stronger ion uptake and more effective adsorption. Among the tested samples, CRAC(0) exhibited the lowest K_d value of 0.35, indicating relatively limited adsorption efficiency. Upon compositing with CuHCF, the K_d values improved significantly: CuHCF/CRAC(0) reached 11.01, CuHCF/CRAC(1) increased to 13.87, and the highest value of 23.41 was observed for CuHCF/CRAC(5). This notable enhancement suggests that the integration of CRAC contributes to improved surface accessibility and structural characteristics, thereby facilitating more efficient cesium ion adsorption. The results confirm the synergistic effect of CRAC and CuHCF in enhancing the overall adsorption performance of the composite materials.

Table 4 summarizes the performance of activated carbon in adsorbing Cs ions from CsCl and Cs-137 solutions. In this study, cassava rhizome activated carbon (CRAC) was prepared *via* hydrothermal carbonization with KMnO$_4$, then composited

Table 4 The comparison performance of activated carbon/MHCF composites for CsCl and Cs-137 adsorption[a]

Material	Synthesis method	Analyze	R (%)	Q_e (mg g^{-1})	Ref.
GO/CS/Cu-PBA	*In situ* synthesis	Cs-137	—	64.7	91
BM/KNiFC	Immobilization	Cs-137	93	—	92
AC/Ni-HCF	Impregnation	Cs-137	98	—	93
CF/CuHCF	Immobilization	CsCl	—	70.3	94
CF/CoHCF	Immobilization	CsCl	—	24.9	94
CF/NiHCF	Immobilization	CsCl	—	37.4	94
MWCNTs/Cu-HCF	Co-precipitation	CsCl	85	310	36
CuHCF/AC	Impregnation	CsCl	—	101.5	23
CuHCF/CRAC(5)	Hydrothermal	Cs-137	99	6.06×10^{-7}	This work

[a] Noted: GO is graphene oxide, CS is chitosan, Cu–PBA is potassium copper hexacyanoferrate(II), BM is biochar, KNiFC is potassium nickel hexacyanoferrate, AC is activated carbon, Ni–HCF is nickel hexacyanoferrate, CF is chitosan fibers, CuHCF and Cu-HCF are copper hexacyanoferrate, CoHCF is cobalt hexacyanoferrate, NiHCF is nickel hexacyanoferrate, and MWCNTs is multiwalled carbon nanotubes.

with CuHCF, resulting in a 99.15% removal efficiency for CuHCF/CRAC(5) after 24 hours. Various synthesis techniques, such as *in situ* synthesis, immobilization, impregnation, activation, and co-precipitation, have previously been employed to produce activated carbon with high Cs$^+$ adsorption capabilities. However, the current study demonstrates superior performance in Cs-137 adsorption, highlighting its strong potential for practical application in wastewater treatment.

Influence of pH on the Cs-137 adsorption

The point of zero charge (pH$_{pzc}$) is the pH at which the surface of a material carries no net electrical charge, indicating a balance between positive and negative surface charges. As shown in Fig. 9a, the pH$_{pzc}$ values for CuHCF, CuHCF/CRAC(0), CuHCF/CRAC(1), and CuHCF/CRAC(5) were approximately 5, 5.5, 7, and 7, respectively. The increase in pH$_{pzc}$ with higher KMnO$_4$ concentrations is attributed to the oxidation-induced functionalization of the carbon surface.[14] Below the pH$_{pzc}$, the adsorbent surface is positively charged, while above this point, it becomes negatively charged.[95]

The acidic or alkaline nature of radioactive wastewater necessitates evaluating the influence of pH on Cs$^+$ ion adsorption.[96,97] As shown in Fig. 9b, the removal efficiency of Cs-137 by CuHCF/CRAC composites was investigated across a pH range of 3 to 12. The results indicate that the maximum removal efficiency
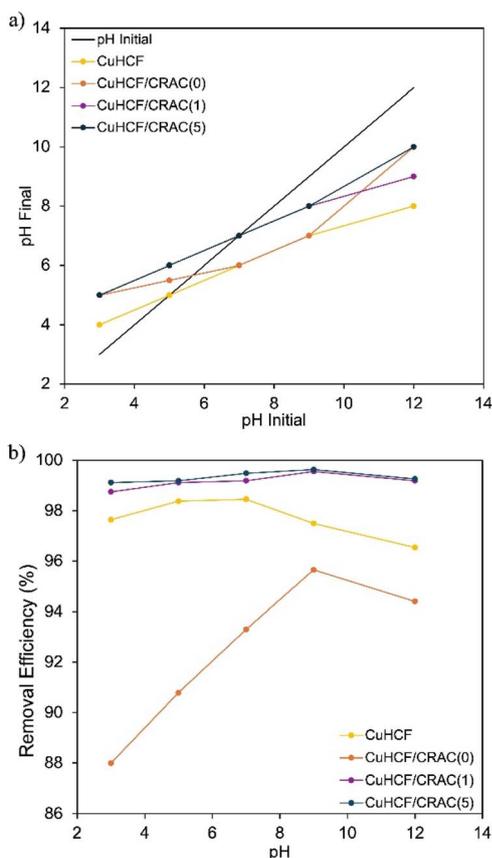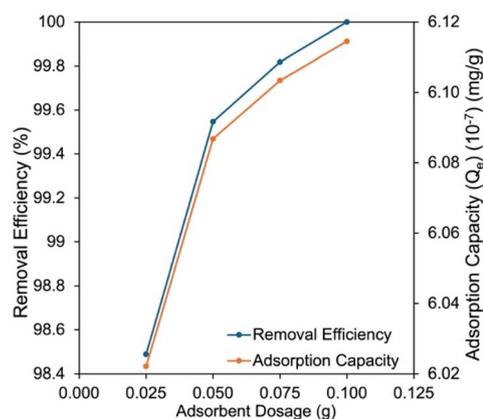

Fig. 10 Effect of adsorbent dosage on the removal efficiency of Cs-137 using CuHCF/CRAC(5) composites over 24 hours.
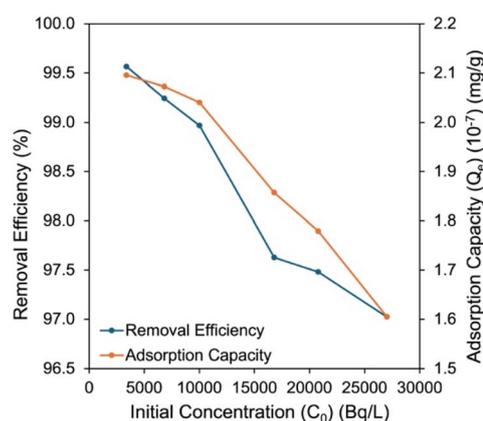

Fig. 11 Effect of initial Cs-137 concentration on its removal efficiency using CuHCF/CRAC(5) composites over 24 hours.

of CuHCF, CuHCF/CRAC(0), CuHCF/CRAC(1), and CuHCF/CRAC(5) is realized at the pH of 7, 9, 9, and 9, respectively. This enhancement is attributed to electrostatic interactions
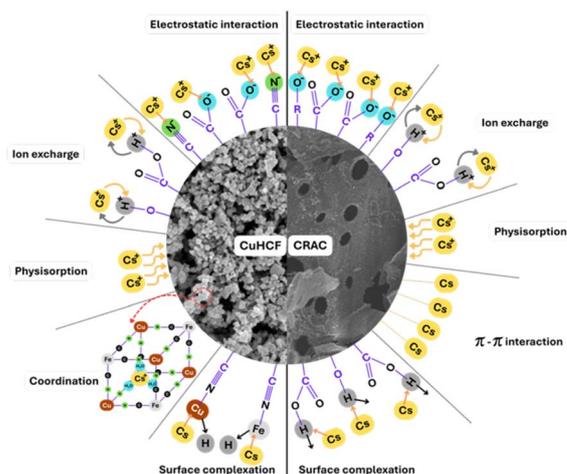

Fig. 9 (a) pH$_{pzc}$ and (b) effect of pH on the Cs-137 adsorption of CuHCF/CRAC composites.

Fig. 12 The possible adsorption mechanism for Cs-137 adsorption onto CuHCF/CRAC composites.

between the positively charged Cs$^+$ ions and the negatively charged adsorbent surface at pH values above the pH$_{pzc}$.[91,98]

Influence of dosage on the Cs-137 adsorption

Fig. 10 illustrates the effect of adsorbent dosage on Cs-137 removal using CuHCF/CRAC(5) composites, tested at varying amounts of 0.025, 0.05, 0.075, and 0.10 g. The experiments were conducted in 10 mL of Cs-137 solution with an initial activity of 10 000 Bq L^{-1} over adsorption period of 24 hours. The results

indicate that complete removal of Cs-137 was achieved at an adsorbent dosage of 0.10 g after 24 hours. This enhanced removal efficiency is attributed to the increased number of active sites available at higher adsorbent masses, which facilitates more effective binding of cesium ions. In essence, as the adsorbent dosage increases, the surface area and number of adsorption sites become sufficient to accommodate all Cs ions present in the solution.[84,85]

Influence of initial concentration on the Cs-137 adsorption

The effect of initial Cs-137 concentration on its adsorption by CuHCF/CRAC(5) composites was examined using 0.05 g of adsorbent in 10.0 mL of Cs-137 solution, with initial concentrations of 3,388, 6,800, 10 015, 16 800, 20 800, and 27 030 Bq L^{-1}. The adsorption experiments were conducted over 24 hours. As shown in Fig. 11, both the removal efficiency and adsorption capacity decreased with increasing initial Cs-137 concentration. This trend is attributed to the saturation of active sites on the adsorbent surface at higher concentrations, where the number of available adsorption sites becomes insufficient to bind all Cs ions present. In other words, the limited quantity of active sites restricts cesium uptake when the solution concentration is high.[85]

Adsorption mechanism

The adsorption of Cs$^+$ onto the CuHCF/CRAC composite adsorbent involves a combination of mechanisms, contributing to its enhanced removal efficiency. Fig. 12 shows the possible adsorption mechanism of Cs-137 onto the CuHCF/CRAC composites. The CRAC surface contains negatively charged functional groups, such as hydroxyl, carbonyl, and carboxyl/carboxylate. Additionally, the CuHCF contains carboxylate (–COO$^-$), cyanide (–C≡N), and carbonyl (–C=O) groups. Adsorption mechanisms of Cs$^+$ removal is primarily driven by the followed:[37,38,91,98–101]

- Electrostatic interaction: the Cs$^+$ ion is attracted to the negatively charged surface groups of the material.
- Ion exchange: the Cs$^+$ ion exchanges with H$^+$ or other cations bound to the surface.
- Surface complexation: the Cs$^+$ ion forms complexes with the functional groups.
- Coordination interaction: the formation of coordination bonds between Cs$^+$ and electron-donating atoms.
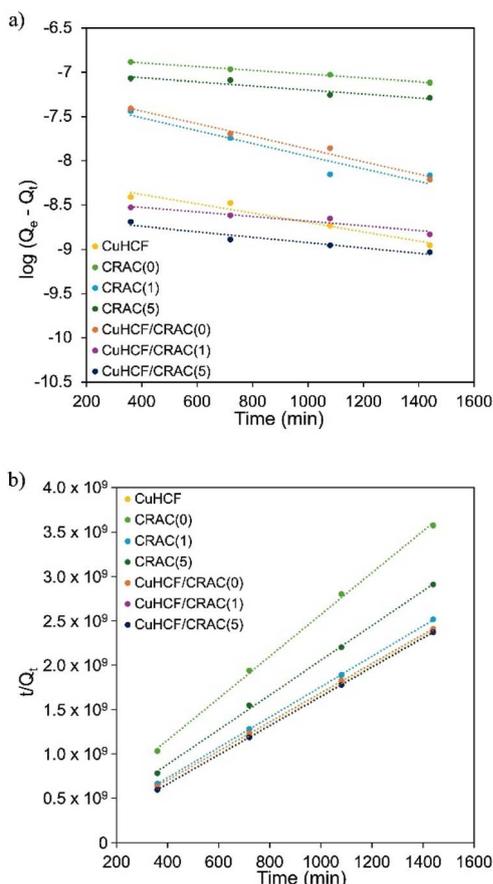

Fig. 13 (a) The linear pseudo-first-order kinetic model and (b) the linear pseudo-second-order kinetic model of all samples for Cs-137 adsorption.

Table 5 The value parameters of adsorption kinetic models for Cs-137 removal[a]

Sample	Q_e (exp) (10^{-7})	Pseudo-first-order			Pseudo-second-order		
		k_1 (10^4)	Q_e (10^6)	R^2	k_2 (10^{-4})	Q_e (10^{-7})	R^2
CuHCF	6.01	12.07	148.66	0.9547	55.20	6.05	1
CRAC(0)	3.89	4.86	6.46	0.9952	2.60	4.24	0.9987
CRAC(1)	5.43	16.58	16.87	0.9072	6.24	5.85	0.9999
CRAC(5)	5.00	5.25	9.34	0.8967	3.84	5.12	0.9991
CuHCF/CRAC(0)	6.01	16.51	14.10	0.9814	5.44	6.10	1
CuHCF/CRAC(1)	6.03	6.01	265.09	0.9208	115.13	6.08	1
CuHCF/CRAC(5)	6.06	7.00	415.43	0.9311	187.23	6.08	1

[a] Note: exp denotes the experiment.

• Physisorption: the preliminary adsorption of Cs^+ ions onto the surface.

• π–π interaction: a non-covalent contact occurring between aromatic rings and π-electron clouds.

These mechanisms work synergistically to enhance Cs^+ removal efficiency, especially when the adsorbent is engineered with high surface area, tailored porosity, and abundant functional groups.

Adsorption kinetics

The adsorption kinetics of Cs-137 removal were investigated to elucidate the underlying adsorption mechanisms on the surfaces of all synthesized samples. To analyze the experimental data, both the pseudo-first-order and pseudo-second-order kinetic models were applied. These models are commonly used to describe the rate and nature of adsorption processes. The kinetic parameters were determined by fitting the experimental data to the respective equations, eqn (8) for the pseudo-first-order model and eqn (9) for the pseudo-second-order model. This approach enabled a comparative evaluation of the adsorption behavior and provided insights into the dominant kinetic mechanisms governing Cs-137 uptake by the adsorbents.[102]

$$\log(Q_e - Q_t) = \log(Q_e) - \left(\frac{k_1}{2.303}\right) \tag{8}$$

$$\frac{t}{Q_t} = \frac{1}{k_2 Q_e^2} + \frac{t}{Q_e} \tag{9}$$

where Q_e is the equilibrium adsorption capacity (mg g^{-1}), Q_t is the adsorption capacity at time (mg g^{-1}), t is time (min), k_1 is the rate constants for the pseudo-first-order kinetic model (min^{-1}), and k_2 is the rate constants for the pseudo-second-order kinetic model (g mg^{-1} min^{-1}). Fig. 13a and b present the kinetic fitting of the pseudo-first-order and pseudo-second-order models for Cs-137 adsorption onto CRAC, CuHCF, and CuHCF/CRAC composites, respectively. The k_1, k_2, Q_e, and determination coefficient (R^2) for all adsorbents were calculated from the slopes and intercepts of the linear plots, as summarized in Table 5. The R^2 values of the pseudo-second-order kinetic model were closer to 1 than those of the pseudo-first-order kinetic model. The results demonstrate that the pseudo-second-order model offers a superior match for these adsorbents, indicating that chemisorption is the predominant process for Cs-137 adsorption.[103,104]

Adsorption isotherms

The adsorption equilibrium of Cs-137 was assessed utilizing the Langmuir, Freundlich, and Temkin isotherms. Fig. 14 illustrates the linearized graphs of the isotherms for Cs-137 adsorption onto CRAC, CuHCF, and CuHCF/CRAC composites. The isotherm parameters obtained from the fitting of each model are presented in Table 6.

The Langmuir isotherm model assumes that adsorption is confined to a monolayer over a homogeneous surface with a finite number of identical sites, devoid of interactions among adsorbed molecules.[18,105] The Langmuir adsorption isotherm model is represented by the subsequent equation:

$$\frac{C_e}{Q_e} = \frac{1}{K_L q_m} + \frac{C_e}{Q_m} \tag{10}$$

where C_e is the concentration of adsorbate solution (mg L^{-1}), Q_e is the equilibrium adsorption capacity of absorbate (mg g^{-1}), K_L is the Langmuir isotherm equilibrium constant (L g^{-1}), and Q_m is the maximum adsorption capacity of absorbate (mg g^{-1}). Fig. 14a presents the linearized Langmuir adsorption isotherm, plotted as C_e/Q_e versus C_e. The low coefficients of determination (R^2) values obtained for all adsorbents, indicated that the
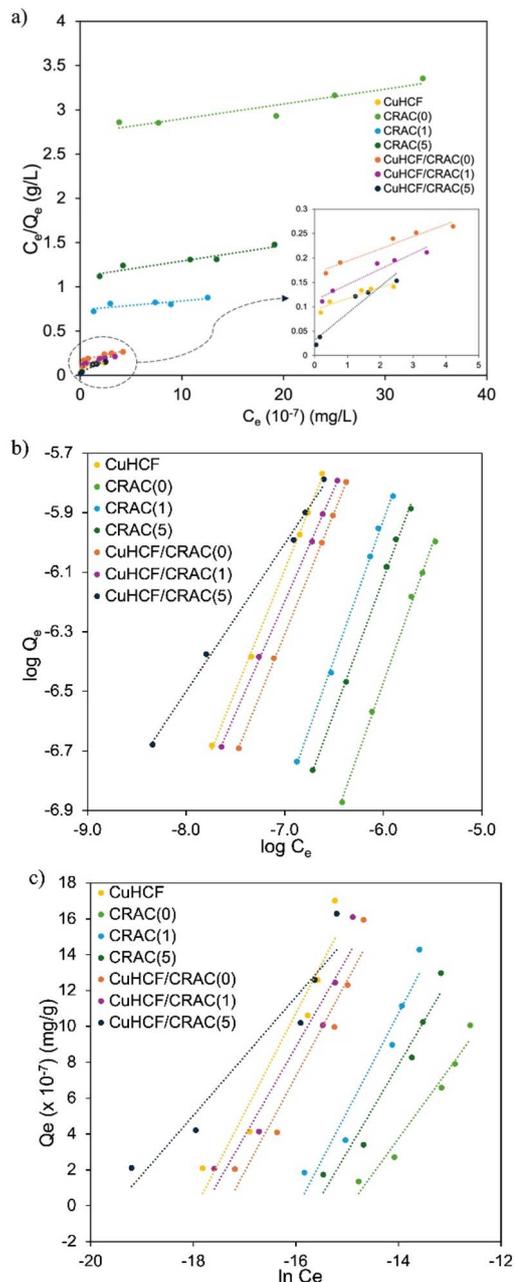

Fig. 14 (a) Langmuir adsorption isotherm, (b) Freundlich adsorption isotherm, and (c) Temkin adsorption isotherm of all samples for Cs-137 adsorption.

Table 6 Value parameters of the Langmuir, Freundlich, and Temkin adsorption isotherms

Sample	Langmuir			Freundlich			Temkin		
	K_L (L mg^{-1})	Q_m (mg g^{-1})	R^2	K_F (L mg^{-1})	n (L mg^{-1})	R^2	K_T (L mg^{-1})	B	R^2
CuHCF	4.12	43.86	0.8661	2.40	1.23	0.9990	61.76	5.53	0.9259
CRAC(0)	162.60	59.52	0.8807	7.38	1.07	0.9979	3.10	3.95	0.9647
CRAC(1)	71.71	97.09	0.7080	2.12	1.07	0.9984	8.51	5.48	0.9414
CRAC(5)	63.43	56.82	0.9123	5.28	1.11	0.9985	6.04	4.88	0.9526
CuHCF/CRAC(0)	6.79	40.16	0.9523	3.93	1.23	0.9998	34.45	5.34	0.9457
CuHCF/CRAC(1)	0.36	31.35	0.9409	8.21	1.32	0.9996	52.58	4.98	0.9434
CuHCF/CRAC(5)	0.57	18.15	0.9320	342.29	2.02	0.9962	301.40	3.30	0.9326

Langmuir isotherm did not adequately describe the adsorption behavior of Cs-137 on the tested adsorbents. This suggests that the adsorption behavior of Cs-137 does not follow the assumptions of monolayer adsorption on a homogeneous surface proposed by the Langmuir isotherm.

The Freundlich adsorption isotherm was commonly applied to describe adsorption processes on heterogeneous surfaces and to account for multilayer adsorption. As an empirical model, it assumes that adsorption occurs on sites with varying affinities and that the adsorption capacity increases with the equilibrium concentration of the adsorbate.[18,105] The Freundlich adsorption isotherm model was expressed by the following equation:

$$\log Q_e = \log K_F + \frac{1}{n}\log C_e \tag{11}$$

where K_F was the Freundlich equilibrium constant (L mg^{-1}), which reflects the adsorption capacity of the adsorbent and n indicates the adsorption intensity or surface heterogeneity. The linear form of the Freundlich isotherm was illustrated by plotting $\log Q_e$ versus $\log C_e$, as displayed in Fig. 14b. The R^2 values derived from the Freundlich isotherm plots were 0.9962 for CuHCF/CRAC(5), 0.9996 for CuHCF/CRAC(1), 0.9998 for CuHCF/CRAC(0), 0.9990 for CuHCF, 0.9985 for CRAC(5), 0.9984 for CRAC(1), and 0.9979 for CRAC(0). The findings reveal a significant correlation nearing 1, implying that these adsorbents align more closely with the Freundlich isotherm model rather than the Langmuir isotherm model. This finding indicates that the adsorption of Cs-137 onto CRAC, CuHCF, and CuHCF/CRAC composites occurs through multilayer adsorption on heterogeneous surfaces.
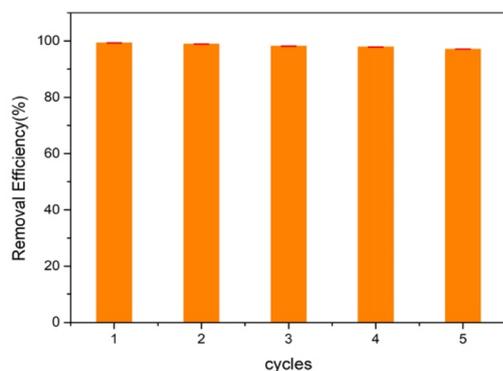
The Temkin adsorption isotherm model effectively describes the interactions between the adsorbent and the adsorbate during the adsorption process. Unlike other models, the Temkin isotherm accounts for indirect interactions among adsorbed species, which influence the adsorption behavior. Which the heat of adsorption decreases linearly with increasing surface coverage due to adsorbate and adsorbate interactions.[18,105] The Temkin adsorption isotherm model was expressed by the following equation:

$$Q_e = B \ln K_T + B \ln C_e \tag{12}$$

where B is the related to binding energy, and K_T is the equilibrium binding constant corresponding to the maximum binding energy. The binding energy can be calculated using the following eqn (13).

$$B = \frac{RT}{b_T} \tag{13}$$

where R is the universal gas constant, T is the absolute temperature, and b_T is the Temkin adsorption isotherm constant. The Temkin adsorption isotherm was plotted as Q_e versus $\ln C_e$, as shown in Fig. 14c. The results showed that the Cs-137 adsorption did not follow the Temkin adsorption isotherm model. It indicated that the interaction between adsorbent and adsorbed species also exists during adsorption process.

Reusability of CuHCF/CRAC composites

The reusability and long-term adsorption performance of the CuHCF/CRAC(5) composites were investigated through successive adsorption–regeneration cycles. Initially, the composite was applied for Cs-137 adsorption and subsequently regenerated by acid treatment with 0.1 M HCl. The regenerated material was then reused for Cs ion adsorption at an initial activity concentration of 10 000 Bq L^{-1}. As shown in Fig. 15, the CuHCF/CRAC(5) composites maintained consistently high Cs-137 removal efficiencies over five consecutive cycles, achieving removal percentages of 99.06%, 98.80%, 98.10%, 97.79%, and 97.06% from the first to the fifth cycle, respectively.

Conclusions

This study successfully developed a high-efficiency composite adsorbent, copper hexacyanoferrate supported on activated carbon derived from cassava rhizomes (CuHCF/CRAC), for the

Fig. 15 Reusability study of the CuHCF/CRAC(5) composites on Cs-137 adsorption.

removal of radioactive cesium-137 (Cs-137) from contaminated wastewater. The preparation method, which involved treating the cassava rhizome with potassium permanganate ($KMnO_4$) *via* a hydrothermal carbonization process, was crucial for enhancing the support matrix. The composite containing the optimized amount of 5% w/w $KMnO_4$ (CuHCF/CRAC(5)) achieved the highest adsorption capability, demonstrating a remarkable Cs-137 removal efficiency exceeding 99% from real wastewater (at 10 000 Bq L^{-1}). This significant improvement in adsorption was primarily attributed to the oxidative modification introduced by the $KMnO_4$ treatment, which provided more accessible surface sites and enhanced structural features on the bio-based activated carbon support, thereby facilitating more efficient capture of cesium ions by the selective CuHCF nanoparticles. The sustained Cs ion removal efficiency of CuHCF/CRAC(5) after multiple adsorption–regeneration cycles confirm its high reusability and practical potential for repeated application in radioactive Cs-137 remediation. The CuHCF/CRAC composites is confirmed to be an efficient, bio-based adsorbent for the removal of radioactive Cs-137 from contaminated wastewater, making it a promising and cost-effective material for application in diverse environmental and industrial contexts.

Author contributions

Kanyanat Tawatbundit: methodology, conceptualization, investigation, data curation, writing-original draft. Sudarat Issarapanacheewin: conceptualization, investigation, validation, writing-review & editing. Witsanu Katekaew: resources. Nikom Prasertchiewchan: resources. Wilasinee Kingkam: investigation. Poonnaphob Sopapan: investigation.

Conflicts of interest

There are no conflicts to declare.

Data availability

All data supporting this study have been included in the article.

Acknowledgements

References

1 M. Silva, A. Bernardes, C. Bergmann, J. Tenório and D. Espinosa, *Ironmaking Steelmaking*, 2008, **35**, 315–320.

2 E. Oliveira Alves, D. Amaro, E. Silva, O. Araujo Filho and K. Alves, *Mater. Res.*, 2018, **21**, e20170779.

3 J. P. Silva, L. R. Martinez and B. H. Costa, *J. Environ. Mater. Res.*, 2023, **45**, 101.

4 K. Yubonmhat, P. Gunhakoon, P. Sopapan, N. Prasertchiewchan and W. Katekaew, *Heliyon*, 2024, **10**, e25792.

5 T. Akharawutchayanon, P. Sopapan, S. Yotthuan, P. Gunhakoon, K. Yubonmhat, S. Issarapanacheewin, W. Katekaew and N. Prasertchiewchan, *Case Stud. Chem. Environ. Eng.*, 2023, **8**, 100409.

6 K. Yubonmhat, T. Akharawutchayanon, P. Nuanjan, S. Issarapanacheewin, W. Katekaew and N. Prasertchiewchan, *J. Hazard., Toxic, Radioact. Waste*, 2022, **26**, 04022009.

7 M. M. Hamed, M. M. S. Ali and A. A. Helal, *Radiochim. Acta*, 2020, **108**, 799–808.

8 S. R. H. Vanderheyden, R. Van Ammel, K. Sobiech-Matura, K. Vanreppelen, S. Schreurs, W. Schroeyers, J. Yperman and R. Carleer, *J. Radioanal. Nucl. Chem.*, 2016, **310**, 301–310.

9 A. Pfeifer and M. Škerget, *Turk. J. Chem.*, 2020, **44**, 859–883.

10 M. M. Sabzehmeidani, S. Mahnaee, M. Ghaedi, H. Heidari and V. A. Roy, *Mater. Adv.*, 2021, **2**, 598–627.

11 A. A. Ahmad, A. Alwahbi, L. A. Al Khateeb and H. Dammag, in *From Biomass to Biobased Products*, ed. E. Jacob-Lopes, L. Queiroz Zepka and R. R. Dias, IntechOpen, London, 2024.

12 S. Yorgun, N. Vural and H. Demiral, *Microporous Mesoporous Mater.*, 2009, **122**, 189–194.

13 N. Kano, M. Pang, Y. Deng and H. Imaizumi, *J. Appl. Solution Chem. Model.*, 2017, **6**, 51–61.

14 S. Issarapanacheewin, K. Tawatbundit, W. Katekaew, N. Prasertchiewchan, W. Kingkam and K. Wangkawong, *J. Hazard., Toxic, Radioact. Waste*, 2026, **30**, 04025032.

15 S. Sawasdee and P. Watcharabundit, *Trends Sci.*, 2025, **22**, 10751.

16 A. Belcaid, B. Beakou, K. El Hassani, S. Bouhsina and A. Anouar, *Water Sci. Technol.*, 2021, **83**, 556–566.

17 S. Kanyakam, W. Pimpa and P. Tansupo, *Int. J. Manage. Appl. Sci.*, 2017, **3**, 1–3.

18 N. S. Sulaiman, M. H. Mohamad Amini, M. Danish, O. Sulaiman and R. Hashim, *Water*, 2021, **13**, 2936.

19 F. O. Kassim, M. Sohail, B. Taylor and O. O. D. Afolabi, *J. Energy Inst.*, 2024, **112**, 101456.

20 G. Phachwisoot, C. Chanthad, K. Nakason, P. Khemthong, S. Youngjan and B. Panyapinyopol, *Asia-Pac. J. Sci. Technol.*, 2023, **28**, 28.

21 S. Khandaker, Y. Toyohara, S. Kamida and T. Kuba, *Water Resour. Ind.*, 2018, **19**, 35–46.

22 H. Moloukhia, W. S. Hegazy, E. A. Abdel-Galil and S. S. Mahrous, *Chem. Ecol.*, 2016, **32**, 324–345.

23 J. Kiener, L. Limousy, M. Jeguirim, J.-M. Le Meins, S. Hajjar-Garreau, G. Bigoin and C. M. Ghimbeu, *Materials*, 2019, **12**, 1253.

24 Q. Tao, X. Zhang, D. Huang, G. Huang, J. Fan, H. Peng, Y. Dai and K. Prabaharan, *J. Radioanal. Nucl. Chem.*, 2019, **322**, 791–799.

25 T. Vincent, C. Vincent and E. Guibal, *Molecules*, 2015, **20**, 20582–20613.

26 D. T. Nguyen, V. T. A. Le, D. P. Truong, T. D. T. Kieu, T. T. H. Nguyen, P. Ning, T. H. G. Duong and K. D. Ho, *Dalat Univ. J. Sci.*, 2021, **11**, 76–97.

27 A. I. Abd-Elhamid, E. M. Abu Elgoud and H. F. Aly, *J. Water Proc. Eng.*, 2024, **57**, 104641.

28 J. Phuriragpitikhon, K. Pluamjai, W. Fuangchoonuch and L. Chuenchom, *IOP Conf. Ser.: Earth Environ. Sci.*, 2023, **1139**, 012003.

29 W. Al Taee, S. Al-Nasri, T. Albayati and I. Salih, *Desalin. Water Treat.*, 2024, **317**, 100121.

30 S. Issarapanacheewin, N. Siangdee, P. Thangsan, W. Katekaew, N. Prasertchiewchan, W. Kingkam and K. Wangkawong, *Electrochem. Commun.*, 2025, **171**, 107857.

31 F. Mbarki, T. Selmi, A. Kesraoui, M. Seffen, P. Gadonneix, A. Celzard and V. Fierro, *Ind. Crops Prod.*, 2019, **140**, 111717.

32 K. Tawatbundit and S. Mopoung, *Materials*, 2022, **15**, 2133.

33 K. R. Pai and J. W. Tester, *Ind. Eng. Chem. Res.*, 2023, **62**, 17562–17576.

34 R. Howeler, *Potassium Agric.*, 1985, 819–841.

35 G. Sun, L. Qiu, M. Zhu, K. Kang and X. Guo, *Ind. Crops Prod.*, 2018, **125**, 41–49.

36 P. Jain, H. Devnani, N. Sandal, S. Nabi, M. A. Bhat and P. P. Ingole, *J. Environ. Chem. Eng.*, 2022, **10**, 106918.

37 A. Takahashi, H. Tanaka, K. Minami, K. Noda, M. Ishizaki, M. Kurihara, H. Ogawa and T. Kawamoto, *RSC Adv.*, 2018, **8**, 34808–34816.

38 R. Chen, H. Tanaka, T. Kawamoto, M. Asai, C. Fukushima, M. Kurihara, M. Ishizaki, M. Watanabe, M. Arisaka and T. Nankawa, *ACS Appl. Mater. Interfaces*, 2013, **5**, 12984–12990.

39 M. Görlin, D. Ojwang, M.-T. Lee, V. Renman, C.-W. Tai and M. Valvo, *ACS Appl. Mater. Interfaces*, 2021, **13**, 59962–59974.

40 Z. Tigrine, O. Benhabiles, L. Merabti, N. Chekir, M. Mellal, S. Aoudj, N. A. Abdeslam, D. Tassalit, S. E. Lebouachera and N. Drouiche, *Sustainability*, 2024, **16**, 9308.

41 F. Chang and H. Li, *Arabian J. Chem.*, 2024, **17**, 105756.

42 V. Thummanatsakun and S. Yampracha, *Int. J. Agric. Technol.*, 2018, **14**, 2137–2150.

43 N. S. Fanelli, L. J. Torres-Mendoza, J. J. Abelilla and H. H. Stein, *Anim. Biosci.*, 2023, **36**, 908–919.

44 Q. Qanytah, K. Syamsu, F. Fahma and G. Pari, *BioResources*, 2020, **15**, 8303–8322.

45 Z. Huang, X. Fang, S. Wang, N. Zhou and S. Fan, *J. Mol. Liq.*, 2023, **373**, 121257.

46 Y. Iradukunda, G. Wang, X. Li, G. Shi, Y. Hu, F. Luo, K. Yi, A. I. M. Albashir, X. Niu and Z. Wu, *J. Energy Storage*, 2021, **39**, 102577.

47 G. Zhang, Y. Sun, P. Zhao, Y. Xu, A. Su and J. Qu, *J. CO2 Util.*, 2017, **20**, 129–140.

48 N. Mojoudi, N. Mirghaffari, M. Soleimani, H. Shariatmadari, C. Belver and J. Bedia, *Sci. Rep.*, 2019, **9**, 19352.

49 A. A. Ceyhan, Ö. Şahin, C. Saka and A. Yalçın, *J. Anal. Appl. Pyrolysis*, 2013, **104**, 170–175.

50 S. Arshad, N. Ngadi, W. Syie Luing, N. A. Saidina Amin, F. Razmi, N. Mohamed, I. Inuwa and A. A. Astimar, *Mal. J. Fund. Appl. Sci.*, 2019, **15**, 1–5.

51 N. Kuperman, A. Cairns, G. Goncher and R. Solanki, *Electrochim. Acta*, 2020, **362**, 35–46.

52 F. Ahmad, W. M. A. W. Daud, M. A. Ahmad, R. Radzi and A. A. Azmi, *J. Environ. Chem. Eng.*, 2013, **1**, 378–388.

53 N. Keppetipola, P. N. Dissanayake, B. Karunarathne, M. Dourges, D. Talaga, L. Servant, C. Olivier, T. Toupance, S. Uchida, K. Tennakone, G. Kumara and L. Cojocaru, *RSC Adv.*, 2021, **11**, 2854–2865.

54 V. Balasubramanian, T. Daniel, J. Henry, G. Sivakumar and K. Mohanraj, *SN Appl. Sci.*, 2019, **2**, 127.

55 M. Hamdy, *Turk. J. Chem.*, 2019, **43**, 94–105.

56 J. Gong, J. Li, J. Xu, Z. Xiang and L. Mo, *RSC Adv.*, 2017, **7**, 33486–33493.

57 A. Daulay, A. Marpongahtun and S. Gea, *S. Afr. J. Chem. Eng.*, 2022, **42**, 32–41.

58 J. Niu, L. Luo, J. Cui, H. Zhang, Y. Guo, L. Li and F. Cheng, *J. Cleaner Prod.*, 2023, **428**, 139374.

59 D. N. Faria, F. S. dos Santos, P. L. Rosa Teixeira, D. F. Cipriano, M. A. Schettino, M. K. de Pietre and J. C. C. Freitas, *Mater. Chem. Phys.*, 2024, **326**, 129813.

60 L. Feng, Z. Xuan, H. Zhao, Y. Bai, J. Guo, C. su and X. Chen, *Nanoscale Res. Lett.*, 2014, **9**, 290.

61 J.-G. Wang, C. Zhang, D. Jin, K. Xie and B. Wei, *J. Mater. Chem. A*, 2015, **3**, 13699–13705.

62 I. Istadi, S. A. Prasetyo and T. S. Nugroho, *Procedia Environ. Sci.*, 2015, **23**, 394–399.

63 P. Jain, S. Jha and P. P. Ingole, *Sustainable Energy Fuels*, 2022, **6**, 1094–1107.

64 S. Srinivasan, L. Kungumadevi, G. Ravi and D. Velauthapillai, *Sci. Rep.*, 2024, **14**, 25760.

65 M. Ghavami, J. Soltan and N. Chen, *Catal. Lett.*, 2021, **151**, 1–15.

66 M. wang, K. Chen, J. Liu, Q. He, G. Li and F. Li, *Catalysts*, 2018, **8**, 138–153.

67 J. G. Outram, S. J. Couperthwaite and G. J. Millar, *J. Environ. Chem. Eng.*, 2018, **6**, 4130–4143.

68 A. Roy, A. Mukhopadhyay, S. Das, G. Bhattacharjee, A. Majumdar and R. Hippler, *Coatings*, 2019, **9**, 551.

69 A. Whitten, D. Guo, E. Tezel, R. Denecke, E. Nikolla and J.-S. McEwen, *JACS Au*, 2024, **4**, 3104–3117.

70 M. Rjeb, A. Labzour, A. Rjeb, S. Sayouri, M. Chafik, E. A, S. Massey and A. Adnot, *Moroc. J. Condens. Matter*, 2004, **5**, 168–172.

71 H. Katsumata, F. Higashi, Y. Kobayashi, I. Tateishi, M. Furukawa and S. Kaneco, *Sci. Rep.*, 2019, **9**, 14873.

72 X. Zhao, S. Sun, Y. Zhang, Y. Wang, Y. Zhu, P. Williams, S. Guan and C. Wu, *Sep. Purif. Technol.*, 2023, **326**, 124866.

73 X.-J. Liu, R. Mao, Z. Huang and R.-J. Xie, *RSC Adv.*, 2015, **5**, 76507–76515.

74 P. Kongsong, M. Masae and A. Jeenarong, *Digest J. Nanomater. Biostruct.*, 2018, **13**, 459–464.

75 M. Kądziołka-Gaweł, M. Czaja, M. Dulski, T. Krzykawski and M. Szubka, *Mineral. Petrol.*, 2021, **115**, 431–444.

76 A. de Morais, J. Alves, A. Lima, M. Lira-Cantu and A. Nogueira, *J. Photonics Energy*, 2015, **5**, 057408.

77 O. M. Nonfodji, J. K. Fatombi, T. A. Ahoyo, B. Boya, L. S. Baba-Moussa and T. Aminou, *Int. J. Hyg. Environ. Health*, 2020, **229**, 113581.

78 S. H. Khalil, M. K. Aroua and W. M. A. W. Daud, *Chem. Eng. J.*, 2012, **183**, 15–20.

79 J. Foungchuen, N. Pairin and C. Phalakornkule, *Appl. Sci. Eng. Prog.*, 2016, **9**, 197–209.

80 M. Keramati and A. A. Ghoreyshi, *Phys. E*, 2014, **57**, 161–168.

81 M. Thommes, K. Kaneko, A. Neimark, J. Olivier, F. Rodriguez-Reinoso, J. Rouquerol and K. Sing, *Pure Appl. Chem.*, 2015, **87**, 1051–1069.

82 K. Chen, T. Zhang, X. Chen, Y. He and X. Liang, *Pet. Explor. Dev.*, 2018, **45**, 412–421.

83 S. Yurdakal, C. Garlisi, L. Özcan, M. Bellardita and G. Palmisano, in *Heterogeneous Photocatalysis*, ed. G. Marcì and L. Palmisano, Elsevier, 2019, pp. 87–152.

84 I. Erwa, O. Ishag, O. A. Alrefaei and I. Hassan, *J. Turk. Chem. Soc., Sect. A*, 2022, **9**, 67–84.

85 H. Priyantini, L. Riadi, C. Effendi, F. Ramadian and A. Mitayani, *IOP Conf. Ser.:Mater. Sci. Eng.*, 2019, **703**, 012015.

86 Y. Zhang, Y. Xiong, Q. Xian, X. He, H. Dan and Y. Ding, *Ann. Nucl. Energy*, 2023, **180**, 109509.

87 Q. Xian, X. He, E. Wang, Z. Bai, D. Zhao, H. Dan, Y. Ding and W. Zhu, *J. Radioanal. Nucl. Chem.*, 2021, **327**, 505–512.

88 T. V. S. L. Satyavani, A. Srinivas Kumar and P. S. V. Subba Rao, *Eng. Sci. Technol. Int. J.*, 2016, **19**, 178–188.

89 K. Byrappa and M. Yoshimura, in *Handbook of Hydrothermal Technology*, ed. K. Byrappa and M. Yoshimura, William Andrew Publishing, Oxford, 2nd edn, 2013, pp. 615–762.

90 Z. Wang, X. Zhang, X. Wang, J. Zhao, J. Yin, G. Wang and Q. Wen, *JOM*, 2025, **77**, 1494–1504.

91 X. Tang, S. Wang, Z. Zhang, Z. Li, L. Wang, L. Yuan, B. Wang, J. Sun, L. Zheng, H. Wang and W. Shi, *Chem. Eng. J.*, 2022, **444**, 136397.

92 T. Asada, N. Sato, T. Ozeki, A. Ito and T. Takase, *Int. J. Environ. Res.*, 2021, **15**, 447–455.

93 S. R. H. Vanderheyden, J. Yperman, R. Carleer and S. Schreurs, *Chemosphere*, 2018, **202**, 569–575.

94 S. Zhuang, K. Zhu, J. Hu and J. Wang, *Sci. Total Environ.*, 2022, **835**, 155575.

95 S. Khandaker, M. F. Chowdhury, M. R. Awual, A. Islam and T. Kuba, *Chemosphere*, 2021, **262**, 127801.

96 M. Gutierrez and H. R. Fuentes, *Appl. Clay Sci.*, 1996, **11**, 11–24.

97 F. Giannakopoulou, C. Haidouti, A. Chronopoulou and D. Gasparatos, *J. Hazard. Mater.*, 2007, **149**, 553–556.

98 J. Nordstrand and L. Kloo, *Phys. Chem. Chem. Phys.*, 2022, **24**, 25452–25461.

99 I. Lee, S.-H. Kim, M. Rethinasabapathy, Y. Haldorai, G.-W. Lee, S. R. Choe, S.-C. Jang, S.-M. Kang, Y.-K. Han, C. Roh, W.-S. Cho and Y. S. Huh, *Sci. Rep.*, 2018, **8**, 4540.

100 E. Allahkarami, A. Dehghan Monfared, L. F. O. Silva and G. L. Dotto, *Sci. Rep.*, 2023, **13**, 167.

101 M. Sultana, M. H. Rownok, M. Sabrin, M. H. Rahaman and S. M. N. Alam, *Clean. Eng. Technol.*, 2022, **6**, 100382.

102 M. Musah, Y. Azeh, J. Mathew, M. Umar Tanko, Z. Abdulhamid and A. Muhammad, *Caliphate J. Sci. Technol.*, 2022, **4**, 20–26.

103 Y. Zhao, C.-W. Cho, L. Cui, W. Wei, J. Cai, G. Wu and Y.-S. Yun, *Environ. Sci. Pollut. Res.*, 2019, **26**, 33897–33905.

104 M. Hamayun, S. Sherazi, S. Zareen, A. Naeem, M. Saeed, K. Shah, A. A. Altaf, S. Murtaza and M. Zubair, *Chiang Mai J. Sci.*, 2018, **45**, 1471–1485.

105 M. Adibmehr and H. Faghihian, *J. Inorg. Organomet. Polym. Mater.*, 2019, **29**, 1941–1955.